IEEE Access
Multidisciplinary ⋮ Rapid Review ⋮ Open Access Journal

Received 9 July 2022, accepted 12 August 2022, date of publication 19 August 2022, date of current version 29 September 2022.

Digital Object Identifier 10.1109/ACCESS.2022.3200385

RESEARCH ARTICLE

A Digital Filter Bank Based Method for Data Reduction in Spaceborne SAR Electronics

HYONIK LEE[1,2], SE-YOUNG KIM[2], SOL KIM[1], (Graduate Student Member, IEEE), AND JONG-WON YU[1], (Member, IEEE)

[1]School of Electrical Engineering, Korea Advanced Institute of Science and Technology (KAIST), Yuseong-gu, Daejeon 34141, Republic of Korea
[2]Defense Space Technology Center, Agency for Defense Development (ADD), Daejeon 34186, Republic of Korea

Corresponding author: Jong-Won Yu (drjwyu67@kaist.ac.kr)

This work was supported by the Research Project for Senior Researcher through the National Research Foundation of Korea (NRF) under Grant 2020R1A2B5B02001696.

ABSTRACT On-board data reduction is a major concern in designing of a spaceborne synthetic aperture radar (SAR) system since the volume of acquired SAR data is generally much higher than the downlink capability to the ground-station. The dechirp-on-receive (DoR) method is considered the state-of-the-art SAR data reduction technique. If there is deramping hardware in the SAR instrument, DoR is an effective method to reduce the volume of images for high resolution modes. In this paper, we use a digital signal processing method which applies a modified discrete Fourier transform (MDFT) filter bank for SAR data reduction. We call this method MDFT band selection filter (MDFT-BSF). This paper presents a quantitative analysis of the MDFT-BSF on data reduction performance. In addition, we provide a relationship between the data reduction performance and the number of sub-bands (M), and show that there is an optimal value of M that minimizes the volume of on-board SAR data. An evaluation of MDFT-BSF including a comparison with the DoR method presents that MDFT-BSF has an advantage for SAR data reduction. We show that MDFT-BSF can be implemented and operated on commercial space-grade FPGAs by the development of a spaceborne SAR digital receiver.

INDEX TERMS Dechirp-on-receive, field programmable gate array, modified discrete Fourier transform filter bank, satellite electronics, synthetic aperture radar.

I. INTRODUCTION

Data reduction is an eternal challenge in the domain of data transmission. The same issue is rising in synthetic aperture radar (SAR) applications as the ceaseless demands for higher resolution and wider swath width on SAR images has made SAR data increasingly larger and more challenging for transmission.

State-of-the-art SAR data reduction technique is the dechirp-on-receive (DoR) method [1]. This method involves generating a linear frequency modulated (LFM) chirp signal and mixing it with the received echo return under the condition that the two signals have the same chirp rate. The mixing operation is generally called a deramping process. The output of the deramping process is a group of sinusoidal signals with the bandwidth estimated as the product of the chirp rate and swath width. If there is deramping hardware in the SAR instrument, DoR has been an effective method for acquiring images from high resolution modes.

The digital signal processing method used in this paper pursues two main goals: not requiring any deramping hardware and possible implementation on commercial space-grade field programmable gate arrays (FPGAs) considering resource-limited applications such as spaceborne SAR. In our method, we apply digital filter bank technology and utilize LFM characteristics of chirp signal for SAR data reduction. We call this method a band selection filter (BSF). Conceptually BSF works as follows. The input signal is divided into time-frequency domain (TFD) blocks based on digital filter bank technology. Then, blocks that only include the region of interest (*RoI*) are selected to be transferred. If the blocks for the *RoI* occupy a relatively small area among

The associate editor coordinating the review of this manuscript and approving it for publication was Ilaria De Munari.

the total TFD blocks of the input signal, BSF can achieve high data reduction. To realize the BSF, a modified discrete Fourier transform (MDFT) filter bank [2], [3], [4], [5], [6] is applied as the best choice of digital filter bank for the BSF. The MDFT filter bank eliminates the alias images from all odd spacing sub-bands providing great signal to noise ratio (SNR) performance. This overcomes the biggest limitation of the popular discrete Fourier transform (DFT) polyphase filter bank [7]. The cosine-modulated filter bank [8], [9], [10], [11], [12] also shows alias cancelation characteristics, but the MDFT filter bank provides a higher computational efficiency for complex input signals [5] which is an important property when considering resource-limited on-board implementation. A patent [13] was proposed to use the MDFT filter bank for on-board SAR reduction, but it only presents the data reduction process. No theoretical analysis results and quantitative comparison to the DoR method are given. In addition, evaluation results and hardware implementation to demonstrate its effectiveness are not provided.

In this paper, we present a quantitative analysis of MDFT-BSF on data reduction performance. To quantify the performance, we define an *RoI* and a region of overhead (*RoO*), and then present the closed form of equations to calculate the size of *RoI* and *RoO* for the MDFT-BSF. Moreover, the closed form of equations to calculate the size of *RoI* and *RoO* from the DoR method is provided for a quantitative comparison with MDFT-BSF. Normally it is expected that the larger number of sub-bands (M) in the digital filter bank results in a smaller size of *RoO* since the frequency width of a TFD block becomes smaller with a larger M. However, this paper proves that there is an optimal value of M to minimize the size of *RoO* according to the parameters of sampling frequency, chirp bandwidth and pulse width.

We present the evaluation results of MDFT-BSF and a performance comparison with the DoR method based on simulation. The evaluation results show that MDFT-BSF has improved data reduction performance compared to the DoR method under the larger swath width to pulse width condition as well as under the SAR mode parameters reflecting real satellite geometry. In addition, we developed a spaceborne SAR digital receiver to show that MDFT-BSF can be implemented and operated on commercial space-grade FPGAs. We used space-qualified EEE-parts and materials to manufacture the SAR digital receiver and completed the space qualification test campaign to confirm that it satisfies the function and performance requirements in space environment conditions [14].

Several studies have focused on data reduction for SAR images. Many of them were focused on quantization techniques such as Block Adaptive Quantization (BAQ) [15], [16], [17], vector quantization (VQ) [18], [19], [20], [21], frequency domain quantization [22] and wavelet transform coding [23]. An approach [24] related to Doppler filtering was also proposed for SAR data reduction. Since MDFT-BSF is a method utilizing the chirp-like signal characteristics for SAR data reduction, it can be used in conjunction with the quantization and Doppler filtering approaches. The dechirp-on-receive technique [25] is a well-known approach also utilizing chirp-like signal characteristics. However, it is only effective when the sampling window for the swath width is much smaller than the pulse width.

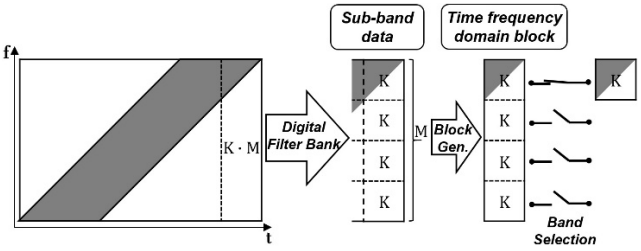

FIGURE 1. Visualization of band selection filter (BSF) concept for on-board filtering process.

This paper is organized as follows. Section II introduces the BSF concept and MDFT-BSF architecture and Section III provides an analysis on the data reduction performance. In Section IV, the data reduction performance evaluation and comparison with DoR are presented. The development of a spaceborne SAR digital receiver, including the implementation of MDFT-BSF on space-grade FPGAs, is given in Section V. Finally, in Section VI, we conclude our study.

II. ARCHITECTURE OF MDFT-BSF

A. BAND SELECTION FILTER

In this section, we describe the filtering concept of the BSF for on-board SAR data reduction. The concept of BSF is visualized in Fig. 1. The first step of BSF is to divide input data into sub-band data via a digital filter bank. The second step is to divide each sub-band data into TFD blocks. If we assume $K \cdot M$ samples flow into the digital filter bank and the number of sub-bands is M, then each TFD block includes K samples. The last step is to select the TFD blocks which are necessary to be transferred, namely band-selection. The reconstruction process is performed from the ground-station in the reverse order of the on-board filtering process.

B. MDFT FILTER BANK

We applied the MDFT filter bank [6] for the digital filter bank shown Fig. 1 due to its computational efficiency and excellent alias cancelation properties.

$$\begin{aligned} H_k(z) &= F_k(z) = H_0\left(zW^k\right) \\ &= z^{-\frac{N-1}{2}} W^{-k\frac{N-1}{2}} P\left(zW^k\right) \\ W^k &= \exp\left(-j\frac{2\pi k}{M}\right) \quad \text{where } k = 0, \ldots, M-1 \end{aligned} \tag{1}$$

Fig. 2 shows an M-channel MDFT filter bank where $H_k(z)$ and $Y_k(z)$ represent the analysis and synthesis filters of the kth sub-band, respectively. $x(n)$ and $y(n)$ shown in the figure are the input and the output of the MDFT analysis filter bank, and $\hat{x}(n)$ indicates the output from the MDFT synthesis filter bank. The zero-phase prototype filter $P(z)$ and the frequency

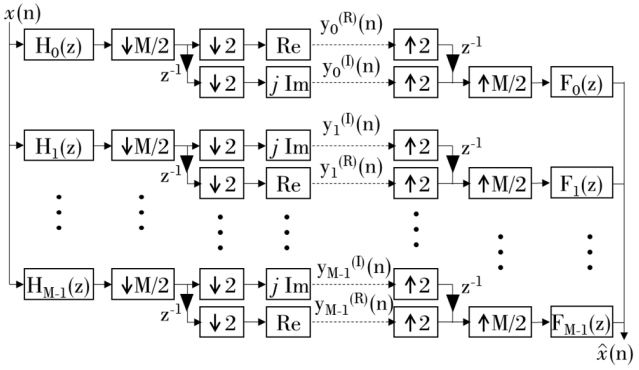

FIGURE 2. M-channel MDFT filter bank.

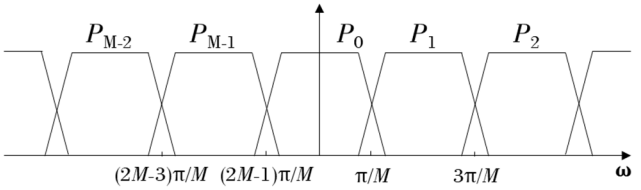

FIGURE 3. Frequency response of filter $P_k(z)$.

shifted version of the prototype filter $P_k(z)$ are presented in Fig. 3. In (1), the sub-band filters $H_k(z)$ and $Y_k(z)$ are the causal version of $P_k(z)$ where N is the filter length of $P(z)$.

The MDFT filter bank shown in Fig. 2 can be realized as illustrated in Fig. 4 by means of two DFT polyphase filter banks where one has a delay of $M/2$ samples. Through this realization, the MDFT filter bank utilizes the computational efficiency of the DFT polyphase filter bank. $E_k(z)$ and $E_k^{(3)}(z)$ denote the kth type-1 and type-3 polyphase filters of $H_0(z)$ respectively.

$$e_k(n) = h_0(n \cdot M + k), \quad k = 0, 1, \ldots, M-1$$
$$e_k^{(3)}(n) = h_0(n \cdot M - k), \quad k = 0, 1, \ldots, M-1$$

The phase factor $W^{-k\frac{N-1}{2}}$ in (1) can be compensated by the factor $W^{k\frac{N-1}{2}}$ on the kth sub-band shown in Fig. 4. The reconstructed signal $\hat{X}(z)$ is written as follows.

$$\hat{X}(z) = \frac{z^{-M/2}}{M} \sum_{k=0}^{M-1} F_k(z) \sum_{l=0}^{M/2-1} H_k\left(zW^{2l}\right) X\left(zW^{2l}\right) \tag{2}$$

(2) shows that all odd spacing aliasing terms of $X(z)$ are perfectly eliminated, including the terms from the neighboring sub-bands. This property significantly reduces the aliasing error in $\hat{X}(z)$.

In [5], it is shown that the operation in analysis and synthesis filters can be simplified and the computational cost for the operation can be significantly reduced by selecting the

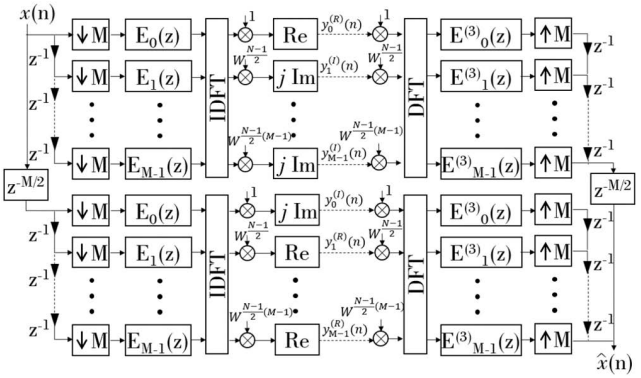

FIGURE 4. MDFT filter bank realized by DFT polyphase filter banks.

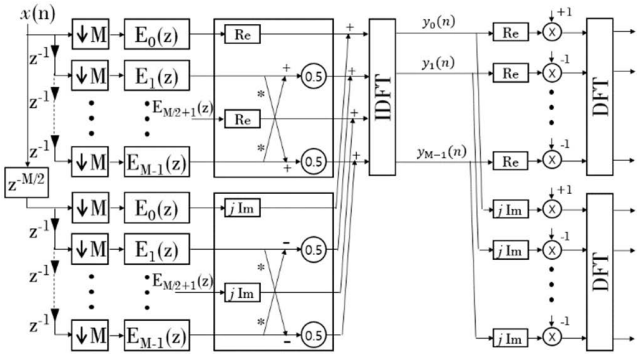

FIGURE 5. Computationally efficient realization of an MDFT analysis filter bank.

appropriate filter length N of $P(z)$ using (3) and (4).

$$\text{if } N = r \cdot M + 1, \quad \text{then } W^{\frac{N-1}{2}k} = (-1)^{rk} \tag{3}$$
$$\text{if } N = r \cdot M + \frac{M}{2} + 1, \quad \text{then } W^{\frac{N-1}{2}k} = (-1)^{rk} \cdot (-i)^k$$
$$\text{where } r = 1, 2, \ldots \tag{4}$$

Fig. 5 illustrates the computationally efficient realization of the MDFT analysis filter bank when we apply (4). It is shown that the two IDFT matrix operations are reduced as one.

The operation for the MDFT synthesis filter bank can also be optimized in the same manner; however, the optimization is not critical for SAR applications since the operation is performed on the ground-station.

C. BAND SELECTION AND BAND RECONSTRUCTION

Here, we present the band selection and the band reconstruction process of MDFT-BSF, as shown in Fig. 6. The output of the MDFT analysis filter bank goes into the block generator. Since some sub-band blocks might not be transferred, there should be a band reconstruction operation before the operation of the synthesis filter bank. The not-transferred sub-band blocks can be generated using zero-value samples. For the band selection operation, the table representing to-be-selected TFD blocks should be pre-defined. A structure of Fig. 7 can be applied to define the band selection table where

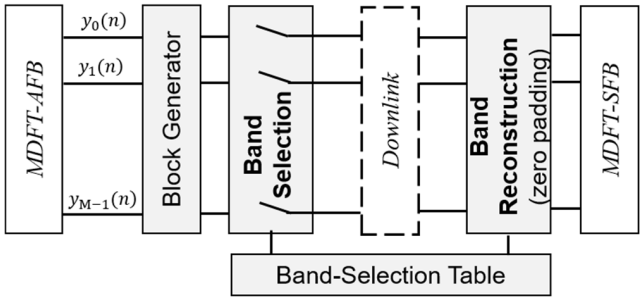

FIGURE 6. Band selection and band reconstruction process of MDFT-BSF.

Sub-Band		
ID	On Time	Duration
0	2	3
1	3	3
2	4	3
3	0	0
4	0	0
5	0	0
6	0	3
7	1	3

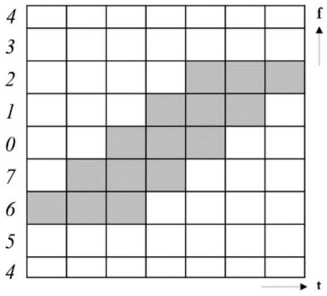

FIGURE 7. Band selection table and time-frequency block representation (example of $M = 8$).

the on-time and the duration are the start location and the number of TFD blocks to be selected, respectively.

III. ANALYSIS ON DATA REDUCTION PERFORMANCE

A. OVERHEAD DATA RATIO OF MDFT-BSF

In this section, we provide an analysis on the data reduction performance of MDFT-BSF. First, we define the Minimum Selection Block (MSB) as the minimum area of the time-frequency domain for the band selection operation.

$$MSB = m \times n, \quad \text{where } m = \frac{F_S}{M} \text{ and } n = K \cdot \frac{M}{F_S} \tag{5}$$

F_S and M indicate the sampling frequency and the number of sub-bands of the MDFT filter bank, respectively. The number of samples n is defined as a multiple of M by considering that the same number of samples are assigned to each sub-band channel operation. Block Adaptive Quantization (BAQ) can be practically applied after the MDFT-BSF on-board operation, so K can be selected as the minimum block size of BAQ.

Fig. 8 presents the time-frequency spectrum of MDFT-BSF. In the figure, B_{EC}, T_{TX}, and T_{SW} are the chirp bandwidth, chirp pulse width and swath width, respectively, where T_{SW} is defined as the time range within the receiving window. The echo return from the near swath to the far swath is represented as the gray area of Fig. 8. Therefore, the gray area and the hatched area in Fig. 8 represent the *RoI* and the *RoO* of the MDFT-BSF, respectively. *Region-A* is the overhead region generated due to the difference between B_{EC} and the frequency range covered by MSBs of the *RoI*. *Region-B* and *Region-C* are the overhead regions created by the difference

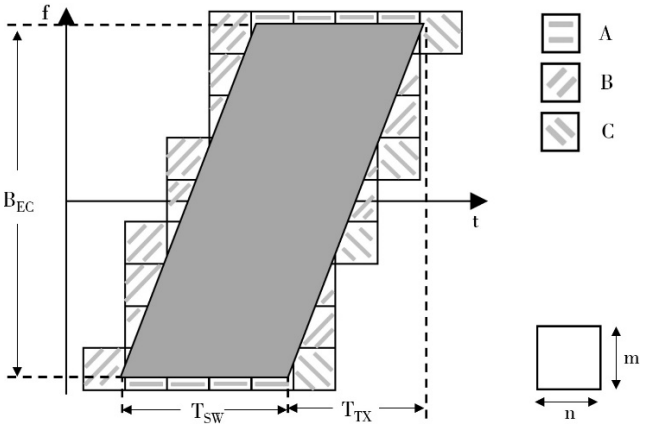

FIGURE 8. Time-frequency spectrum of MDFT-BSF.

between T_{SW} and the time range covered by the MSBs of the *RoI*.

Normally, we can define T_{SW} as a multiple of n. The centers of the near swath and the far swath can then be located at the centers of the first and the last MSBs in the center sub-band. For simplicity, let us consider the upper half side of B_{EC}. As seen in Fig. 8, we can recognize that one MSB overhead is needed for each sub-band when the near (or far) swath passes through the upper side of the MSB. Both the overhead from the near swath side and the far swath side make one MSB overhead for each sub-band. This region is defined as Region-B. When the near (or far) swath passes through the right side of the MSB, additional MSB overheads are required for the sub-band. If the chirp rate is gentle compared to the MSB, several MSB overheads are needed for the same sub-band. This overhead region is defined as *Region-C*.

$$RoI = B_{EC} \times T_{SW} \tag{6}$$

$$RoO = (Region\ A) + (Region\ B) + (Region\ C) \tag{7}$$

Let us define I as the minimum number of MSBs covering the frequency range of B_{EC}. As B_{EC} increases I increases from 1 to *M-1* by two and finally becomes M. Let us define J as the number that the near (or far) swath pass through the side of MSB within T_{TX}. As T_{TX} increases J increases by two.

$$I = \begin{cases} 2 \cdot \left\lceil \dfrac{B_{EC}}{2m} + 0.5 \right\rceil - 1, \\ \quad where\ 0 \le B_{EC} \le \dfrac{M-1}{M} F_S \\ M, \\ \quad where\ B_{EC} > \dfrac{M-1}{M} F_S \end{cases} \tag{8}$$

$$J = 2 \cdot \left\lfloor \frac{1}{2} \cdot \left(\frac{T_{TX}}{n} + 1 \right) \right\rfloor \tag{9}$$

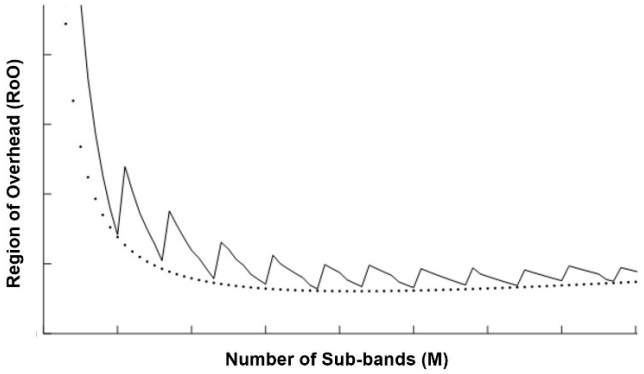

FIGURE 9. Region of overhead w.r.t. M.

Region-A, *Region-B* and *Region-C* are calculated using (8) and (9) as follows.

$$\begin{aligned}&(Region\ A)\\&= (m \cdot I - B_{EC}) \cdot T_{SW}\\&= \begin{cases} (F_S - B_{EC}) \cdot T_{SW}, \\ \quad where\ B_{EC} > \dfrac{M-1}{M} F_S \\ \left\{ \dfrac{F_S}{M} \cdot \left(2 \cdot \left\lceil \dfrac{B_{EC} \cdot M}{2F_S} + 0.5 \right\rceil - 1 \right) - B_{EC} \right\} \cdot T_{SW}, \\ \quad where\ 0 \le B_{EC} \le \dfrac{M-1}{M} F_S \end{cases}\end{aligned} \tag{10}$$

$$\begin{aligned}&(Region\ B)\\&= n \cdot m \cdot I\\&= \begin{cases} K \cdot M, \\ \quad where\ B_{EC} > \dfrac{M-1}{M} F_S \\ K \cdot \left(2 \cdot \left\lceil \dfrac{B_{EC} \cdot M}{2F_S} + 0.5 \right\rceil - 1 \right), \\ \quad where\ 0 \le B_{EC} \le \dfrac{M-1}{M} F_S \end{cases}\end{aligned} \tag{11}$$

$$(Region\ C) = n \cdot m \cdot J = 2K \cdot \left\lfloor \frac{1}{2} \cdot \left(\frac{F_S \cdot T_{TX}}{K \cdot M} + 1 \right) \right\rfloor \tag{12}$$

We define the ratio of *RoI* as R_{RoI} and the ratio of *RoO* as R_{RoO} based on the maximum area of the time-frequency domain. R_{RoI} and R_{RoO} indicate the interest data ratio and the overhead data ratio, respectively. For MDFT-BSF, they can be calculated using (6), (7), (10), (11) and (12). In (13) and (14), T_{RX} is the receiving window length which is the sum of T_{TX} and T_{SW}.

$$(Ratio\ of\ RoI) = R_{RoI} = \frac{RoI}{F_S \cdot T_{RX}} \tag{13}$$

$$(Ratio\ of\ RoO) = R_{RoO} = \frac{RoO}{F_S \cdot T_{RX}} \tag{14}$$

$$where\ T_{RX} = T_{TX} + T_{SW}$$

B. APPROXIMATION AND ANALYSIS

Interestingly, from (11) and (12) we can find that, as M increases, *Region-B* increases; however, *Region-C* decreases. This indicates that there is an optimal value of M which minimizes the *RoO*.

Since there are ceiling and floor operations in the equation of *RoO*, it becomes a saw tooth shape as a function of *M,* as shown in Fig. 9. Let's define an approximated function $RoO_{low}(M)$ which passes through the bottom of the teeth of *RoO(M)*. Then, we find M which minimizes $RoO_{low}(M)$.

1) IN CASE OF $B_{EC} > \frac{M-1}{M} F_S$, *namely* $M < \frac{F_S}{F_S - B_{EC}}$

Let $0 \le \beta < 1$, then

$$(Region\ A) = (F_S - B_{EC}) \cdot T_{SW} \tag{15a}$$

$$(Region\ B) = K \cdot M \tag{15b}$$

$$\begin{aligned}(Region\ C) &= 2K \cdot \left(\frac{1}{2} \cdot \left(\frac{F_S \cdot T_{TX}}{K \cdot M} + 1 \right) - \beta \right)\\&= K \cdot (1 - 2\beta) + \frac{F_S \cdot T_{TX}}{M}\end{aligned} \tag{15c}$$

In the case of $\beta = 1$, *Region-C* has the minimum value and *RoO(M)* locates at the bottom of the teeth. Therefore, we can define $RoO_{low}(M)$ as follows.

$$\begin{aligned}RoO_{low}(M) = K \cdot M + \frac{F_S \cdot T_{TX}}{M} + (F_S - B_{EC})\\ \cdot\ T_{SW} - K\end{aligned} \tag{15d}$$

By differentiating $RoO_{low}(M)$ into M, we can find the value of M minimizing $RoO_{low}(M)$.

$$\frac{d}{dM}\left(RoO_{low}(M)\right) = K - \frac{F_S \cdot T_{TX}}{M^2} \tag{15e}$$

Let $d(\mathrm{RoO_{low}}(M))/dM = 0$, then

$$M = \sqrt{\frac{F_S \cdot T_{TX}}{K}}, \quad where\ M < \frac{F_S}{F_S - B_{EC}} \tag{15f}$$

We can also define an overhead data ratio, $R_{RoO\_low}(M)$, given as (15g) using (15d), and $(R_{RoO\_low})_{min}$ by inserting M from (15f) into (15g) as follows.

$$\begin{aligned}&R_{RoO\_low}(M)\\&= \frac{RoO_{low}(M)}{F_S \cdot T_{RX}}\\&= \frac{K \cdot M}{F_S \cdot T_{RX}} + \frac{T_{TX}}{T_{RX} \cdot M} + \frac{(F_S - B_{EC}) \cdot T_{SW} - K}{F_S \cdot T_{RX}}\end{aligned} \tag{15g}$$

$$\begin{aligned}&\left(R_{RoO\_low}\right)_{min}\\&= \frac{1}{T_{RX}} \left(2 \cdot \sqrt{\frac{K \cdot T_{TX}}{F_S}} - \frac{B_{EC} \cdot T_{SW} + K}{F_S} + T_{SW} \right)\end{aligned} \tag{15h}$$

2) IN CASE OF $0 \le B_{EC} \le \frac{M-1}{M}F_S$, *namely* $M \ge \frac{F_S}{F_S - B_{EC}}$
Let $0 \le \alpha < 1$ and $0 \le \beta < 1$, then

(Region A)

$$= \left\{ \frac{F_S}{M} \cdot \left(2 \cdot \left(\frac{B_{EC} \cdot M}{2F_S} + 0.5 + \alpha \right) - 1 \right) - B_{EC} \right\} \cdot T_{SW} = \frac{2\alpha \cdot F_S \cdot T_{SW}}{M} \tag{16a}$$

(Region B)

$$= K \cdot \left(2 \cdot \left(\frac{B_{EC} \cdot M}{2F_S} + 0.5 + \alpha \right) - 1 \right) = 2\alpha \cdot K + \frac{K \cdot B_{EC} \cdot M}{F_S} \tag{16b}$$

(Region C)

$$= K \cdot (1 - 2\beta) + \frac{F_S \cdot T_{TX}}{M} \tag{16c}$$

In the case of $\alpha = 0$ and $\beta = 1$, *RoO(M)* is located at the bottom of the teeth. Therefore, we can define RoO_{low}(M) as follows.

$$RoO_{low}(M) = \frac{K \cdot B_{EC} \cdot M}{F_S} + \frac{F_S \cdot T_{TX}}{M} - K \tag{16d}$$

By differentiating $RoO_{low}(M)$ into M, we can find the value of M minimizing $RoO_{low}(M)$.

$$\frac{d}{dM}\left(RoO_{low}(M)\right) = \frac{K \cdot B_{EC}}{F_S} - \frac{F_S \cdot T_{TX}}{M^2} \tag{16e}$$

Let $d(RoO_{low}(M))/dM = 0$, then

$$M = F_S \cdot \sqrt{\frac{T_{TX}}{K \cdot B_{EC}}}, \quad where\ M \ge \frac{F_S}{F_S - B_{EC}} \tag{16f}$$

We can also define $R_{RoO\_low}(M)$ given as (16g) using (16d), and $(R_{RoO\_low})_{min}$ by inserting M from (16f) into (16g) as follows.

$$R_{RoO\_low}(M) = \frac{RoO_{low}(M)}{F_S \cdot T_{RX}} = \frac{K \cdot B_{EC} \cdot M}{F_S^2 \cdot T_{RX}} + \frac{T_{TX}}{M \cdot T_{RX}} - \frac{K}{F_S \cdot T_{RX}} \tag{16g}$$

$$\left(R_{RoO\_low}\right)_{min} = \frac{1}{F_S \cdot T_{RX}} \left(2 \cdot \sqrt{K \cdot B_{EC} \cdot T_{TX}} - K \right) \tag{16h}$$

(15f) and (16f) help the analysis of the optimal value of M that minimizes *RoO(M)*. The optimal M is independent of T_{SW}. It is proportional to $\sqrt{F_S \cdot T_{TX}}/K$. In the case of $0 \le B_{EC} \le \frac{M-1}{M}F_S$, the optimal M becomes as large as $\sqrt{F_S}/B_{EC}$ compared to the $B_{EC} > \frac{M-1}{M}F_S$ case. Moreover, (16h) helps for the analysis of the minimum overhead data ratio for $0 \le B_{EC} \le \frac{M-1}{M}F_S$. The minimum R_{RoO} is inversely proportional to F_S, and it decreases as T_{SW} increases under the condition of the same T_{TX}.

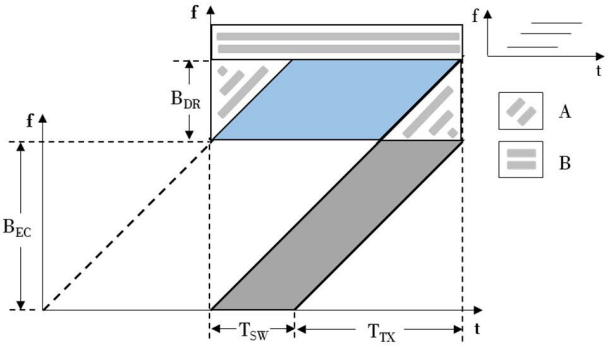

FIGURE 10. Time-frequency spectrum of DoR.

C. COMPARISON TO DECHIRP-ON-RECEIVE

Fig. 10 presents the time-frequency spectrum of the DoR method. In the figure, B_{EC}, T_{TX}, T_{SW} and B_{DR} are the chirp bandwidth, chirp pulse width, swath width and bandwidth after the deramping process, respectively. The gray area represents the *RoI* before the deramping process. The blue and the hatched area represent the *RoI* and the *RoO* after the deramping process, respectively. *Region-A* is the overhead region included in the spectrum of the deramped signal and *Region-B* is the overhead region existing due to over-sampling.

$$RoI = B_{EC} \cdot T_{SW} \tag{17}$$

$$RoO = (Region\ A) + (Region\ B) \tag{18}$$

According to (6) and (17), the deramping process does not change the *RoI* size. Let σ be the over-sampling factor. Then, the interest data ratio and overhead data ratio are obtained as follows.

$$(Ratio\ of\ RoI) = R_{RoI} = \frac{RoI}{F_S \cdot T_{RX}} \tag{19}$$

$$(Ratio\ of\ RoO) = R_{RoO} = \frac{B_{EC} \cdot T_{SW}}{F_S \cdot T_{RX}} \cdot \left(\frac{T_{RX} \cdot \sigma}{T_{TX}} - 1 \right) = \frac{B_{EC} \cdot r}{F_S} \cdot \left(\sigma - \frac{1}{1+r} \right), r = \frac{T_{SW}}{T_{TX}} \tag{20}$$

$$(Ratio\ of\ RoI\ and\ RoO) = R_{RoI} + R_{RoO} = \frac{B_{EC} \cdot T_{SW} \cdot \sigma}{F_S \cdot T_{TX}} \tag{21}$$

(20) shows that the R_{RoO} increases as B_{EC}/F_S or T_{SW}/T_{TX} increases. From (21), we can see that in the case of $T_{SW} \cdot \sigma > T_{TX}$, the data size becomes bigger than before the deramping process. The detailed performance evaluation between MDFT-BSF and DoR is shown in Section IV.

IV. EVALUATION OF MDFT-BSF

In this section, we present the evaluation results and discuss the performance of MDFT-BSF. First, we explain the data reduction performance of MDFT-BSF with different sets of

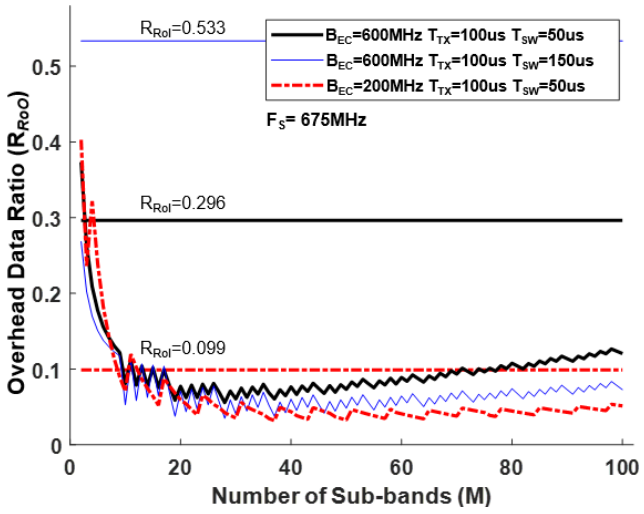

FIGURE 11. Overhead data ratio over number of sub-bands(M) with different sets of B_{EC}, T_{TX} and T_{SW} at $Fs = 675$MHz.

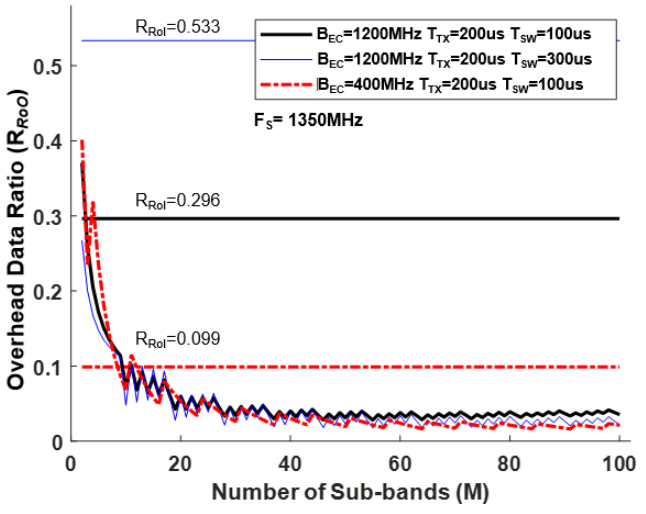

FIGURE 12. Overhead data ratio over number of sub-bands(M) with different sets of B_{EC}, T_{TX} and T_{SW} at $Fs = 1350$MHz.

parameters. Next, we compare the performance of MDFT-BSF with that of the DoR method. During the evaluation, we assume the over-sampling factor of DoR is 1.1 and K of MDFT-BSF is 128.

A. MDFT-BSF DATA REDUCTION PERFORMANCE

Fig. 11 shows R_{RoI} and R_{RoO} as a function of M. In this simulation, we assume Fs=675MHz and consider three sets of B_{EC}, T_{TX}, and T_{SW} conditions. The case of $B_{EC} = 600$MHz, $T_{TX} = 100$us and $T_{SW} = 50$us (Case1) is chosen as a reference. We then change the T_{SW} to 150us (Case2), and then B_{EC} to 200MHz (Case3). The figure shows that R_{RoI} of the three cases are 0.296, 0.533 and 0.099, respectively. Namely, a longer swath width and larger bandwidth create a higher interest data ratio. As we expect from Section III, the envelope of R_{RoO} decreases and then increases as M increases. The minimum values of R_{RoO} for the three cases are 0.056, 0.035 and 0.032 at $M = 28$, 28 and 37, respectively. The change of swath width does not change the value of the optimal M. We can find that R_{RoO} changes little for M above a certain value. For example, $M = 23$ gives just about 1% higher R_{RoO} than the optimal M for the three cases. The figure also shows that the longer swath width and smaller bandwidth result in a lower R_{RoO}, as we expected from (16h) with the $M \geq \frac{F_S}{F_S - B_{EC}}$ condition.

As shown in Figure 12, we increase Fs to 1350MHz and change B_{EC}, T_{TX}, and T_{SW} with the same rate. In general, Fig. 12 gives similar results to Fig. 11. The R_{RoI} is the same as the values in Fig. 11. However, the R_{RoO} is generally lower than the values in Fig. 11 with larger values of M. At $M =$ 55, 55 and 91, the minimum R_{RoO} becomes 0.028, 0.018 and 0.016, respectively. This shows that the data ratio is optimized at a larger value of M when Fs increases. We can also find that $M = 37$ gives nearly a 0.5% higher R_{RoO} than the optimal M for the three cases.

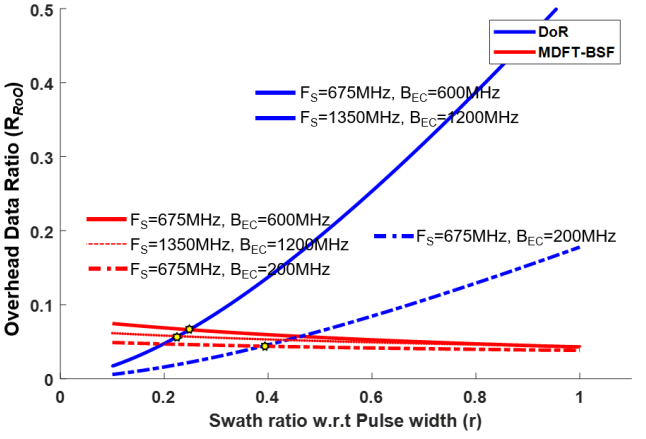

FIGURE 13. Overhead data ratio comparison between MDFT-BSF and DoR method with different Fs and B_{EC}.

B. COMPARISON TO DECHIRP-ON-RECEIVE

In Fig. 13, we compare the data reduction performance of MDFT-BSF and DoR as the ratio of swath width to pulse width increases. Let $r = T_{SW}/T_{TX}$. For this simulation, the case of $F_S = 675$MHz, $B_{EC} = 600$MHz and $T_{TX} = 100$us (Case1) is chosen as a reference. We then change the B_{EC} to 200MHz (Case2) and F_S to 1350MHz (Case3). The values of M are chosen as even numbers, 28 and 56, obtained from the previous simulation results. The figure shows that the R_{RoO} of DoR increases as r increases, but the R_{RoO} of MDFT-BSF decreases. It also shows that the variation of R_{RoO} in MDFT-BSF is minor compared to DoR. The R_{RoO} crossing occurs at $r = 0.25$ for Case1. This indicates that the data reduction performance of MDFT-BSF becomes superior to DoR as swath width is longer than 0.25 of the pulse width. For the other two cases, the R_{RoO} crossing occurs at $r = 0.39$ and $r = 0.225$ respectively. In addition, if the ratio of B_{EC} to Fs is

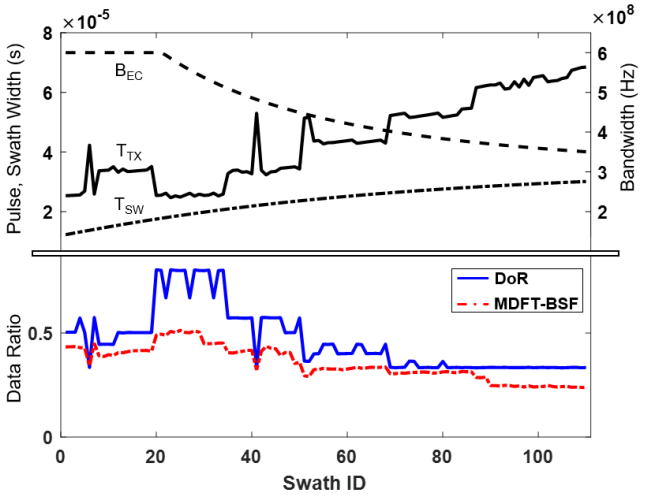

FIGURE 14. Data ratio comparison between the MDFT-BSF and DoR method w.r.t. designed parameters for high resolution modes reflecting satellite geometry.

the same, the R_{RoO} of DoR has the same value, but the R_{RoO} of MDFT-BSF decreases with a larger Fs.

Fig. 14 shows the data reduction performance of MDFT-BSF and DoR in practical scenario cases. For this simulation, we design the parameters for high resolution modes considering a real satellite geometry. PRFs are selected based on the PRF diagram, and the Swath ID in the figure represents a different incidence angle. In this simulation, we assume decimation operation after the deramping process, and the decimation ratio is designed as follows by considering real implementation. For MDFT-BSF, $M = 16$ and $K = 128$ are used.

$$(\textit{decimation ratio}) = [1\ 1.25\ 1.5\ 1.75\ 2\ 2.25\ 2.5\ 2.75\ 3]$$

From the figure, MDFT-BSF presents better performance in general. As Fig. 14 shows, the difference increases when T_{SW}/T_{TX} becomes larger. From these parameters, DoR requires a 1.315 times higher average data ratio than MDFT-BSF.

V. HARDWARE IMPLEMENTATION

We demonstrate that MDFT-BSF can be implemented and operated on space-grade FPGAs by developing a spaceborne SAR digital receiver (DRX). Since these FPGAs are commercially available, implementation on FPGAs is much less expensive than implementation on application specific integrated circuits (ASICs). All the EEE-parts and materials used in DRX are space qualified, and through a space qualification test campaign, it is confirmed that all functions and performance of DRX are satisfied with the requirements under conditions considering the space environment [14].

Fig. 15 shows the flow of processing received signals in the DRX. Signals down-converted to the baseband from SAR Radio Frequency Equipment (RFE) are the DRX input. The amplitude of the input signals is adjusted through an amplifier

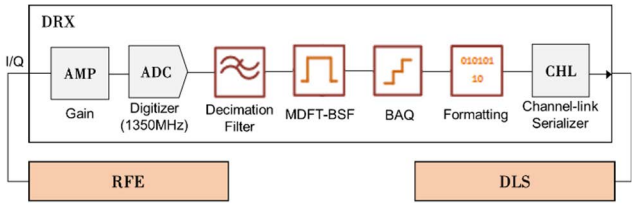

FIGURE 15. Functional block diagram of signal processing flow in the SAR digital receiver.

considering the dynamic range of the ADCs. DRX uses 10-bit ADCs to digitize the input I/Q signals at a 1350MHz sampling rate. According to the bandwidth of the input signals, the sampling rate of the digitized data is adjusted through the decimation filter and MDFT-BSF.

In our SAR mode design, MDFT-BSF is used for high-resolution modes; for the other modes such as standard modes and wide-swath modes, the decimation filter is used and MDFT-BSF is bypassed. Since the decimation ratio is high in the other modes, the decimation filter shows sufficient data reduction performance; however, MDFT-BSF requires relatively high resource usage and computation. The output data from MDFT-BSF is compressed by BAQ. After being packetized in the Consultative Committee for Space Data Systems (CCDS) format, it is transmitted through the channel-link interface to the Datalink (DLS) subsystem, which is transmission equipment to the ground-station.

Fig. 16 shows the functional block diagram of FPGAs used in DRX. Two FPGAs are assigned to implement data processing functions between ADCs and the Channel-link serializers shown in Fig. 15. Xilinx Virtex4 is selected for the FPGAs since it has space heritage indicating that it has previously been used in space. The functional blocks presented in Fig. 15 are allocated considering the available resources of FPGA1 and FPGA2. Accordingly, the functional blocks of MDFT-BSF are divided into MDFT-BSF(A) and MDFT-BSF(B).

Xilinx suggests that Virtex4 is manufactured through a 90nm copper CMOS process and can operate with a clock frequency of 350MHz or higher [26]. However, it is necessary to design with a clock frequency sufficiently lower than this for the stable use of FPGAs. FPGA1 is designed to operate at two clock frequencies by dividing the functional blocks into the front and rear ends. The input stage of FPGA1 applies a 4-parallel Double Data Rate (DDR) structure of 168.75 (=1350/8) MHz clock frequency. The decimation filter is designed as a two-stage serial structure, and the ratio is selectable considering the received signal bandwidth. MDFT-BSF applies a 3-parallel structure with a 120MHz clock frequency that can process up to 360 MS/s. The 120MHz clock frequency is decided after a trade-off between the FPGA power consumption and the system rx-duty cycle which is the sampling window length over the pulse repetition interval. Then, BAQ is applied to compress the data with a selectable ratio among 10:8/6/5/4.

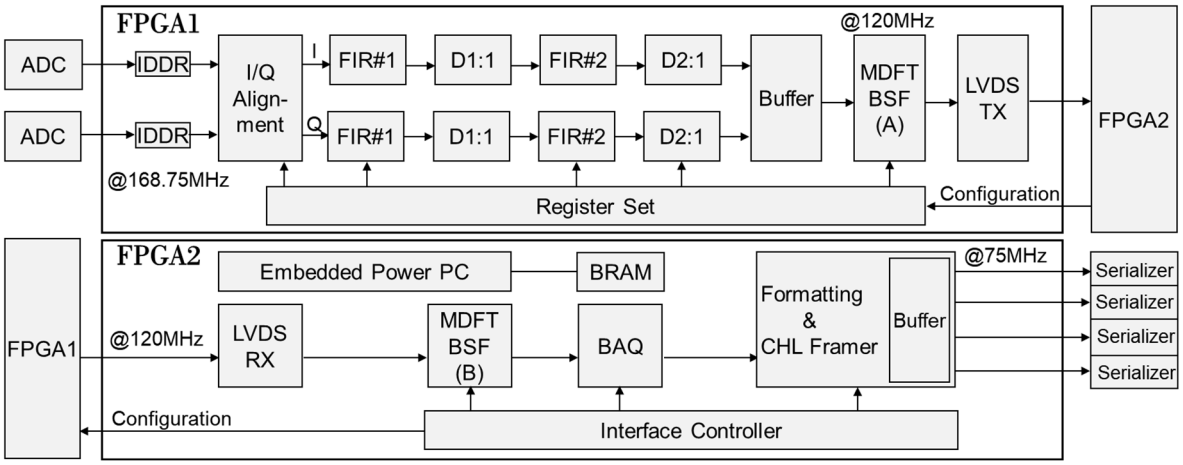

FIGURE 16. Functional block diagram of FPGAs in DRX.

TABLE 1. Resource usage of FPGA1 and FPGA2.

Type	Logic	Used	Available	Utilization
LX200	LUT	80,491	178,176	44%
	Flip Flop	82,290	178,176	46%
	DSP Slice	54	96	56%
	BRAM	162(2,916Kb)	336(6,048Kb)	48%
FX140	LUT	95,686	126,336	75%
	Flip Flop	68,692	126,336	54%
	DSP Slice	96	192	50%
	BRAM	524(9,432Kb)	552(9,936Kb)	94%

The internal functions of MDFT-BSF are implemented in FPGA1 and FPGA2, as shown in Fig. 17. Considering the sequential processing of the functional blocks presented in Fig. 15, the resources are insufficient to implement the entire MDFT-BSF functions in an FPGA; therefore, its functions are divided into two FPGAs, as shown in Fig. 17. The number of sub-bands (M) is set to 16 which requires 24 delays and 32 filter banks. The 'Re, Im' blocks represent an operation 'extracting real and imaginary parts' and the 'Sub, Add, 1/2' blocks indicate 'Subtraction, Addition and Division by 2' operation, respectively. The blocks are configured to reflect the operation shown in Fig. 5.

Table 1 shows the resource usage of FPGA1 and FPGA2 in their final FPGA images. We use LX200 and FX140 among the Virtex4 space families for FPGA1 and FPGA2, respectively. This selection is based on an analysis of the required resources. As shown in Table 1, LX200 has more resources in logic slices which include look-up tables and flip-flops, and FX140 has more resources in BRAMs [26]. Since our initial design of data processing function for FPGA1 requires more logic slices than the final design, we select LX200. In LX200, only the first-stage decimation filter is implemented with DSP slices. The remaining filters are implemented with LUTs since the total number of DSP slices is insufficient.

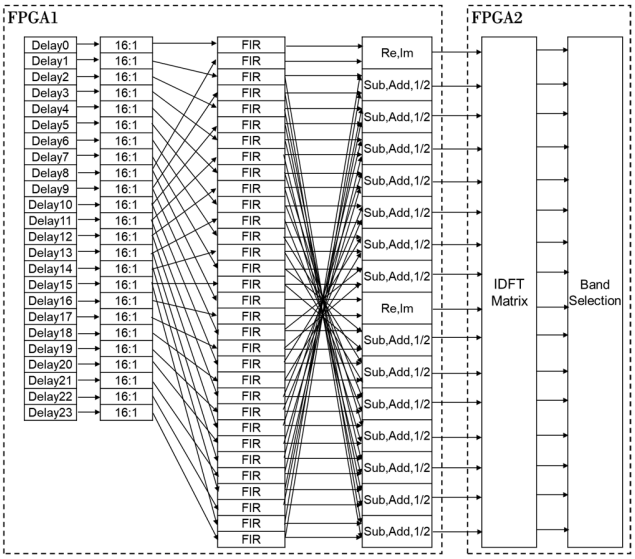

FIGURE 17. MDFT-BSF on-board implementation in FPGA1 and FPGA2.

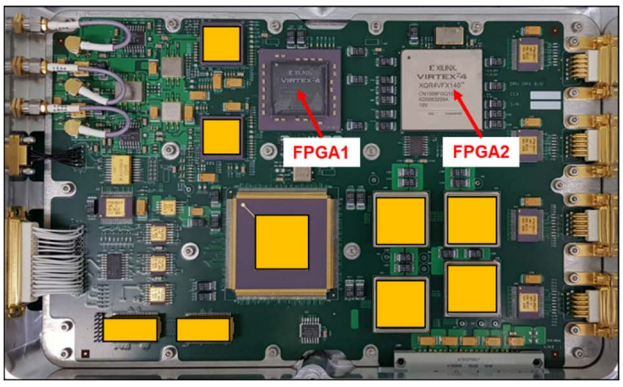

FIGURE 18. Manufactured spaceborne SAR DRX.

Fig. 18 shows the manufactured DRX. All the EEE-parts and the materials used in the DRX are space qualified. Moreover, we developed a digital receiver unit (DRU) which

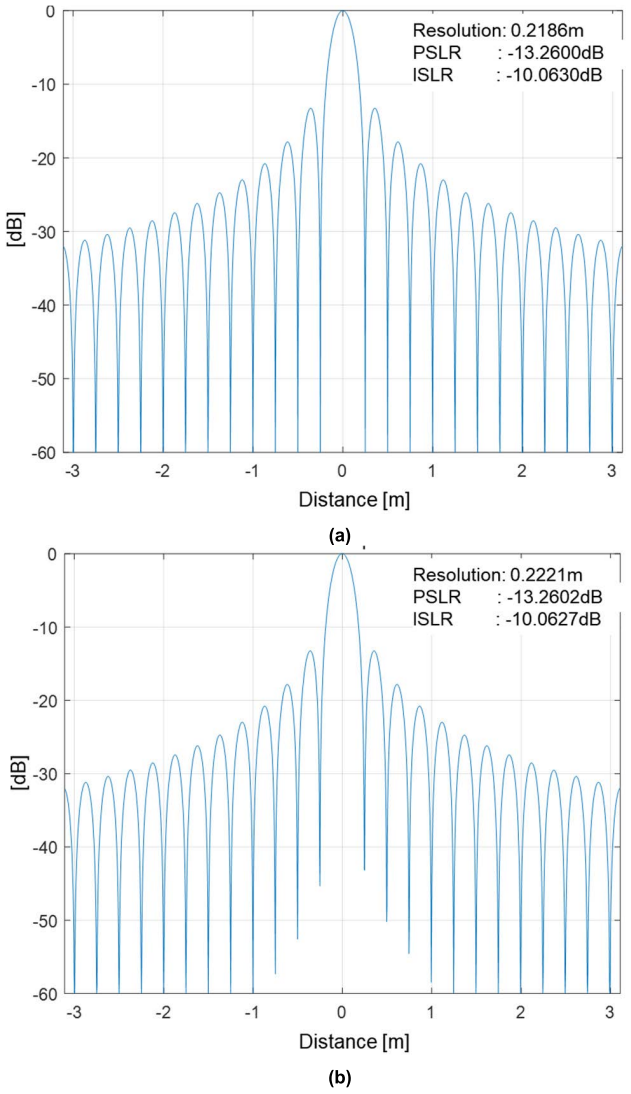

FIGURE 19. Impulse response function performance of DRX. (a) without MDFT-BSF and (b) with MDFT-BSF.

TABLE 2. Impulse response function comparison according to MDFT-BSF application in DRX.

	IDEAL	w/o MDFT-BSF	w/ MDFT-BSF
Resolution(m)	0.2186	0.2186	0.2221
PSLR(dB)	-13.2613	-13.2600	-13.2602
ISLR(dB)	-10.0619	-10.0630	-10.0627

consists of four DRXs and two power suppliers. The DRU has completed a qualification test campaign and all functions and performance requirements for the DRU have been confirmed to be satisfactory for satellite environment conditions.

Fig. 19 and Table 2 show the impulse response function (IRF) performance from the restored chirps at the DRX output. This is the result of compression with a relative pulse, and a weighting function is not applied. The first column shows an ideal case for reference purposes, and the second and third columns show a case in which MDFT-BSF is not applied in DRX and one in which it is, respectively. In this test, the BAQ is bypassed and the DRX input signal is generated by an arbitrary waveform generator (AWG). Although there is a slight deterioration in resolution when MDFT-BSF is applied, it has little effect on IRF characteristics.

VI. CONCLUSION

In this paper, we present an MDFT-BSF architecture to utilize an MDFT filter bank for on-board SAR data reduction. This paper presents a quantitative analysis of MDFT-BSF on data reduction performance. We provide the closed form of equations to calculate the size of data via MDFT-BSF and prove there is an optimal value for the number of sub-bands (M) which minimizes the data size. The evaluation results show that MDFT-BSF has better data reduction performance compared to the DoR method under SAR mode parameters reflecting real satellite geometry. The data reduction performance of MDFT-BSF shows little change according to the ratio of swath width to pulse width, but the performance of DoR decreases as the ratio increases. Our development of a spaceborne SAR digital receiver demonstrates that MDFT-BSF is fully applicable to commercial space-grade FPGAs.

REFERENCES

[1] G. Carrara, R. S. Goodman, and R. M. Majewski, *Spotlight Synthetic Aperture Radar*. Norwood, MA, USA: Artech House, 1995.
[2] N. J. Fliege, "Computational efficiency of modified DFT polyphase filter banks," in *Proc. 27th Asilomar Conf. Signals, Syst. Comput.*, Nov. 1993, pp. 1296–1300.
[3] N. J. Fliege, "Modified DFT polyphase SBC filter banks with almost perfect reconstruction," in *Proc. IEEE Int. Conf. Acoust., Speech Signal Process.*, vol. 2. Adelaide, SA, Australia, Apr. 1994, pp. 149–152.
[4] T. Karp and N. J. Fliege, "MDFT filter banks with perfect reconstruction," in *Proc. Int. Symp. Circuits Syst.*, Seattle, WA, USA, May 1995, pp. 744–747.
[5] T. Karp and N. J. Fliege, "Computationally efficient realization of MDFT filter banks," in *Proc. 8th Eur. Signal Process. Conf.*, Trieste, Italy, Sep. 1996, pp. 1–4.
[6] T. Karp and N. J. Fliege, "Modified DFT filter banks with perfect reconstruction," *IEEE Trans. Circuits Syst. II, Analog Digit. Signal Process.*, vol. 46, no. 11, pp. 1404–1414, Nov. 1999.
[7] M. G. Bellanger and J. L. Daguet, "TDM-FDM transmultiplexer: Digital polyphase and FFT," *IEEE Trans. Commun.*, vol. COM-22, no. 9, pp. 1199–1205, Sep. 1974.
[8] T. A. Ramstad and J. P. Tanem, "Cosine-modulated analysis-synthesis filterbank with critical sampling and perfect reconstruction," in *Proc. Int. Conf. Acoust., Speech, Signal Process.*, Toronto, ON, Canada, May 1991, pp. 1789–1792.
[9] R. D. Koilpillai and P. P. Vaidyanathan, "Cosine-modulated FIR filter banks satisfying perfect reconstruction," *IEEE Trans. Signal Process.*, vol. 40, no. 4, pp. 770–783, Apr. 1992.
[10] R. A. Gopinath and C. S. Burrus, "Theory of modulated filter banks and modulated wavelet tight frames," in *Proc. IEEE Int. Conf. Acoust. Speech Signal Process.*, Minneapolis, MN, USA, Apr. 1993, pp. 169–172.
[11] Y.-P. Lin and P. P. Vaidyanathan, "Linear phase cosine modulated maximally decimated filter banks with perfect reconstruction," *IEEE Trans. Signal Process.*, vol. 43, no. 11, pp. 2525–2539, Nov. 1995.
[12] T. Q. Nguyen and R. D. Koilpillai, "The theory and design of arbitrary-length cosine-modulated filter banks and wavelets, satisfying perfect reconstruction," *IEEE Trans. Signal Process.*, vol. 44, no. 3, pp. 473–483, Mar. 1996.
[13] T. Becker, "Reduction of receive data of a radar, in particular, a synthetic aperture radar," Patent EP 14 003 841 A, Nov. 14, 2014. [Online]. Available: https://www.epo.org/

[14] S. J. Kang, S. W. Park, H. Y. Choi, G. H. Ryu, J. P. Kim, S. H. Jung, S. Y. Kim, H. I. Lee, and H. U. Oh, "Thermo-mechanical design and validation of spaceborne high-speed digital receiver unit for synthetic aperture radar application," *Aerospace*, vol. 8, pp. 1–19, Oct. 2021.
[15] R. Kwok and W. T. K. Johnson, "Block adaptive quantization of Magellan SAR data," *IEEE Trans. Geosci. Remote Sens.*, vol. 27, no. 4, pp. 375–383, Jul. 1989.
[16] T. Algra, "Data compression for operational SAR missions using entropy-constrained block adaptive quantisation," in *Proc. IEEE Int. Geosci. Remote Sens. Symp.*, vol. 2. Toronto, ON, Canada, Jun. 2002, pp. 1135–1138.
[17] E. Attema, C. Cafforio, M. Gottwald, P. Guccione, A. M. Guarnieri, F. Rocca, and P. Snoeij, "Flexible dynamic block adaptive quantization for Sentinel-1 SAR missions," *IEEE Geosci. Remote Sens. Lett.*, vol. 7, no. 4, pp. 766–770, Oct. 2010.
[18] Y. Linde, A. Buzo, and R. M. Gray, "An algorithm for vector quantizer design," *IEEE Trans. Commun.*, vol. COM-28, no. 1, pp. 84–95, Jan. 1980.
[19] J. W. Owens, M. W. Marcellin, B. R. Hunt, and M. Kleine, "Compression of synthetic aperture radar video phase history data using trellis-coded quantization techniques," *IEEE Trans. Geosci. Remote Sens.*, vol. 37, no. 2, pp. 1080–1085, Mar. 1999.
[20] P. A. Chou, T. Lookabaugh, and R. M. Gray, "Entropy-constrained vector quantization," *IEEE Trans. Acoust., Speech, Signal Process.*, vol. 37, no. 1, pp. 31–42, Jan. 1989.
[21] T. R. Fischer and M. Wang, "Entropy-constrained trellis-coded quantization," *IEEE Trans. Inf. Theory*, vol. 38, no. 2, pp. 415–426, Mar. 1992.
[22] U. Benz, K. Strodl, and A. Moreira, "A comparison of several algorithms for SAR raw data compression," *IEEE Trans. Geosci. Remote Sens.*, vol. 33, no. 5, pp. 1266–1276, Sep. 1995.
[23] V. Pascazio and G. Schirinzi, "Wavelet transform coding for SAR raw data compression," in *Proc. IEEE Int. Geosci. Remote Sens. Symp.*, vol. 4. Hamburg, Germany, Jun. 1999, pp. 2251–2253.
[24] M. Villano, G. Krieger, and A. Moreira, "Onboard processing for data volume reduction in high-resolution wide-swath SAR," *IEEE Geosci. Remote Sens. Lett.*, vol. 13, no. 8, pp. 1173–1177, Aug. 2016.
[25] R. J. C. Middleton, "Dechirp-on-receive linearly frequency modulated radar as a matched-filter detector," *IEEE Trans. Aerosp. Electron. Syst.*, vol. AES-48, no. 3, pp. 2716–2718, Jul. 2012.
[26] *Space-Grade Virtex-4QV Family Overview, DS658, V2.1*, Xilinx, San Jose, CA, USA, Nov. 2014.

HYONIK LEE received the B.S. degree in electrical engineering and the M.S. degree in computer science from the Korea Advanced Institute of Science and Technology (KAIST), Daejeon, Republic of Korea, in 2002 and 2005, respectively, where he is currently pursuing the Ph.D. degree in electrical engineering.

Since 2008, he has been a Senior Researcher with the Agency for Defense Development (ADD), Daejeon. His current research interests include spaceborne synthetic aperture radar system design, data compression and quantization theory, and on-board signal processing.

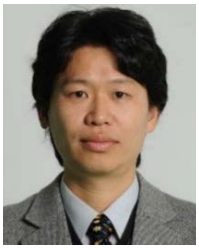

SE-YOUNG KIM received the Ph.D. degree in electrical engineering from the Korea Advanced Institute of Science and Technology (KAIST), Daejeon, Republic of Korea, in 2010.

Since 1993, he has been a Chief Principal Researcher with the Agency for Defense Development (ADD), Daejeon. His current research interests include spaceborne synthetic aperture radar system design, recent SAR acquisition technique for high resolution and wide swath, and precise calibration technique improving the radiometric and geometric accuracy.

SOL KIM (Graduate Student Member, IEEE) received the B.S. degree in radio engineering from Chungnam National University (CNU), in 2018, and the M.S. degree in electrical engineering from the Korea Advanced Institute of Science and Technology (KAIST), Daejeon, South Korea, in 2020, where he is currently pursuing the Ph.D. degree in electrical engineering.

His current research interests include microwave power transmission (MPT), RF energy harvesting, phased array, beamforming, radio wave propagation, RADAR systems, calibration, RF system applications, and antenna design.

JONG-WON YU (Member, IEEE) received the B.S., M.S., and Ph.D. degrees in electrical engineering from the Korea Advanced Institute of Science and Technology (KAIST), Daejeon, South Korea, in 1992, 1994, and 1998, respectively.

From 2000 to 2001 and from 2001 to 2004, he was also with Wide Telecom Head and Telson, South Korea. From 2004 to 2013, he was with KAIST, initially as an Assistant Professor of electrical engineering and as an Associate Professor. He is currently a Professor with KAIST. His research interests include emphasize microwave/millimeter-wave circuits (monolithic microwave integrated circuits (MMICs), hybrid), wireless communication systems, and RFID/ubiquitous sensor networks.